Supporting Information

Regulation of dual-atom doping porous carbon towards high-performance capacitive storage devices

Jizhao Zou[a], Zhewen Deng[a], Jingyou Xu[a], Shunhong Chen[b], Xin Yu[c], Hongliang Wu[a], Fenglin Zhao[b]*

[a] Shenzhen Key Laboratory of Special Functional Materials & Shenzhen Engineering Laboratory for Advance Technology of Ceramics, College of Materials Science and Engineering, Shenzhen University, Shenzhen 518060, China

[b] School of Mechanical Engineering, Chengdu University, Chengdu 610106, China

[c] Capxon electronic technology CO., LTD. Shenzhen, China

*Corresponding Author: Fenglin Zhao

E-mail: zhaoflin@163.com

Electrochemical calculations

The specific capacitance of CGX electrode materials (C_{3g}, F g^{-1}) for supercapacitor energy storage was calculated from GCD and CV curves by equations S1 and S2.

$$C_{3g} = I \times \Delta t / (m \times \Delta V) \quad \text{(S1)}$$

$$C_{3g} = \int_{V_a}^{V_b} I(V)dV \Big/ 2m \times v \times \Delta V \quad \text{(S2)}$$

Where I, m, Δt, v, and ΔV represent the current (A), active material mass of the single electrode (g), time (s), scan rate (V s^{-1}) and voltage window (V), respectively.

The specific capacitance of the symmetrical supercapacitor (C_{2g}, F g^{-1}) was obtained from GCD discharge time based on equation S3. The energy density E (Wh kg^{-1}) and power density P (W kg^{-1}) of the supercapacitor device were calculated through equations S4 and S5, respectively.

$$C_{2g} = 4 \times I \times \Delta t / (m \times \Delta V) \quad \text{(S3)}$$

$$E = C_{2g} \times \Delta V^2 / (8 \times 3.6) \quad \text{(S4)}$$

$$P = 3600 \times E / \Delta t \quad \text{(S5)}$$

The capacity (C, mAh g^{-1}) of the zinc ion capacitor is estimated from GCD discharge time by equation S6.

$$C = I \times \Delta t / (3.6 \times m) \quad \text{(S6)}$$

Where I, m, and Δt represent the current (A), active material mass of the electrode (g), and discharge time (s), respectively.

Density functional theory calculation details

The Vienna ab-initio simulation package plane-wave code was utilized the spin-polarized density DFT calculations within the generalized gradient approximation through Perdew-Burke-Ernzerhof process [1-3]. The projected augmented wave potential was employed to describe the ionic cores, and the plane wave basis cutoff energy of valence electrons was set as 500 eV [4, 5]. The valence electron

configurations utilized in this work are $4s^2 3d^{10}$ (Zn), $2s^2 2p^2$(C), $2s^2 2p^4$ (O), and $2s^2 2p^3$ (N), respectively. Partial occupancies of the Kohn-Sham orbitals were utilized through the Gaussian smearing method within the width of 0.02 eV. The energy change lower than 10^{-6} eV was the qualification of electronic energy self-consistent. This slab model was separated by a 15 Å vacuum layer in the z-direction. A 3×3×1 gamma-point centered k-point grid for the Brillouin zone was used as the structural optimization of the surface model. In addition, all atomic layers consented to the full relaxation.

The adsorption energy (E_{ads}) of an adsorbate zinc atom was defined as the following:

$$E_{ads} = E_{ads/surf} - E_{surf} - E_{ads} \quad \text{(S7)}$$

Where $E_{ads/surf}$, E_{surf}, and Eads represent the energy of the adsorbate adsorbed on a surface slab, surface slab energy, and adsorbate energy, respectively.

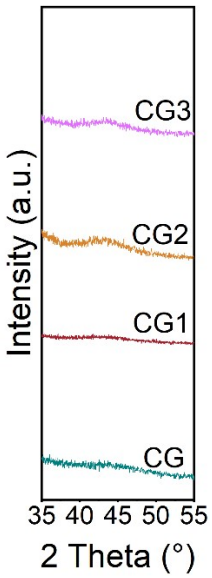

Fig. S1. XRD patterns at 35~55°.

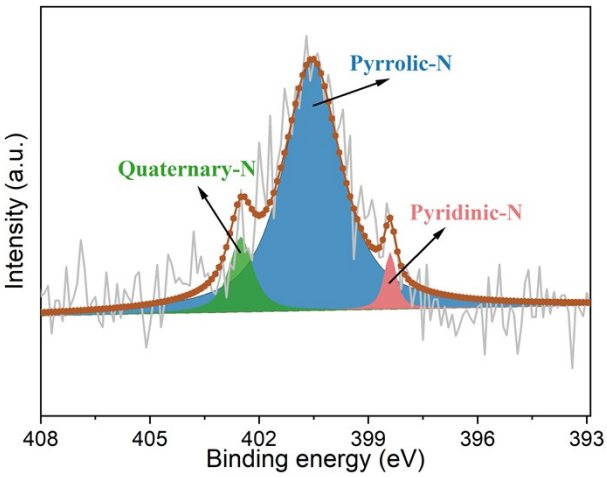

Fig. S2. N1s spectra of CG2.

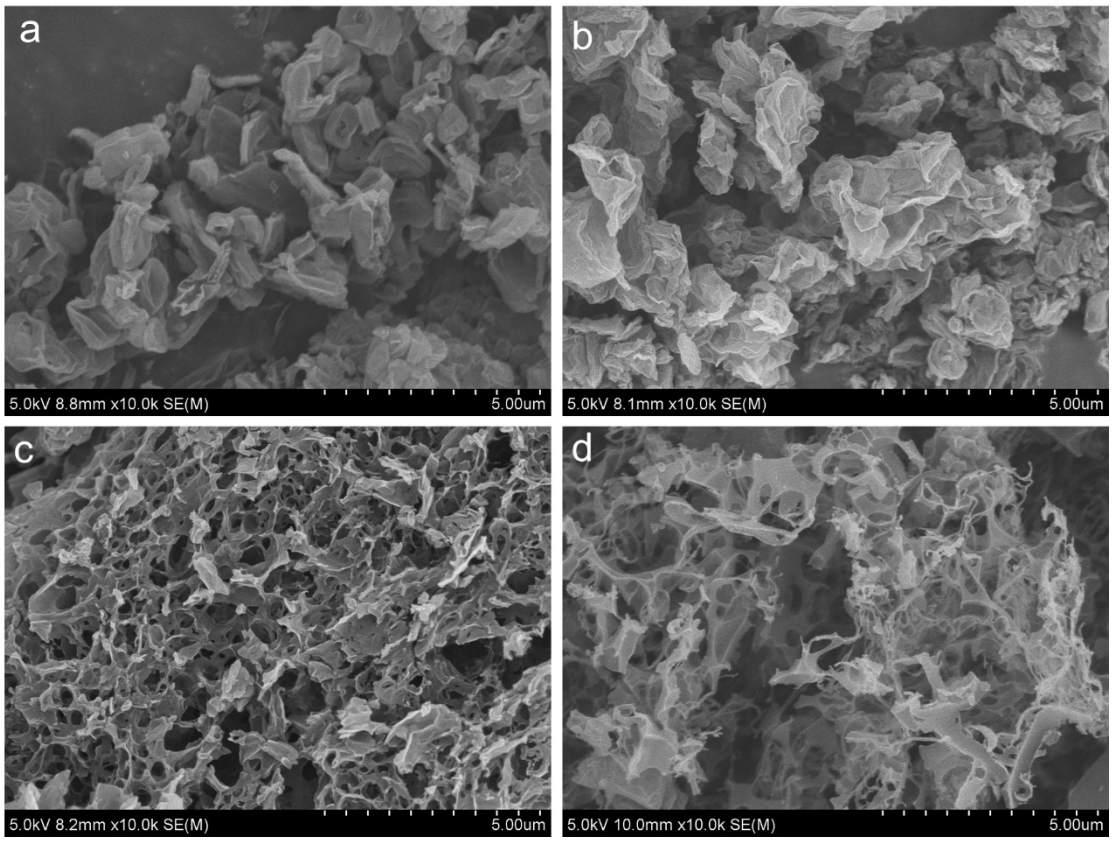

Fig. 3. SEM images of CGX, (a) CG, (b) CG1, (c) CG2, and (d) CG3.

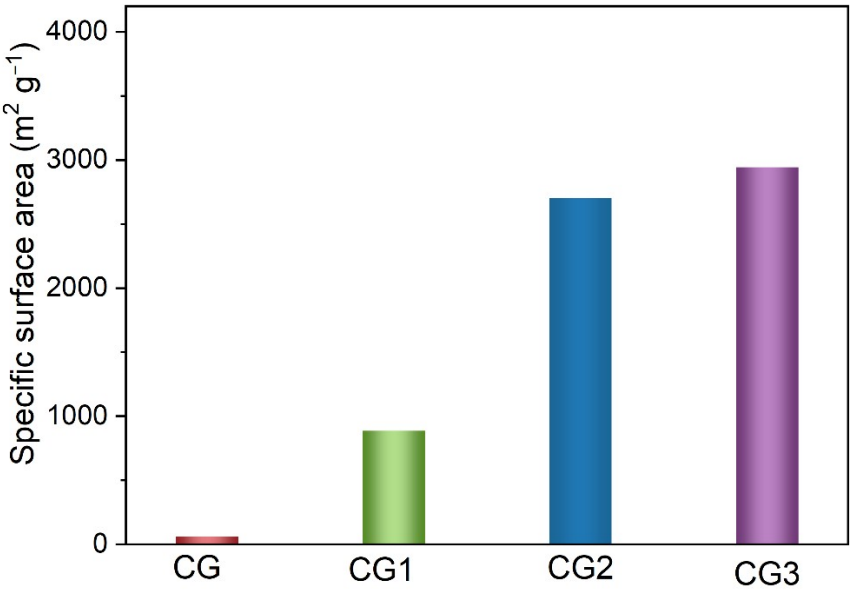

Fig. S4. The specific surface area of CGX samples.

Table S1. The specific surface area and volume parameters of samples.

Sample	S_{BET} (m^2g^{-1})	S_{micro} (m^2g^{-1})	S_{micro}/S_{BET} (%)	V_{total} (cm^3g^{-1})	V_{micro} (cm^3g^{-1})	V_{meso} (cm^3g^{-1})	V_{macro} (cm^3g^{-1})
CG	62.9	36.4	57.9	0.12	0.02	0.07	0.03
CG1	886.2	511.8	57.8	1.08	0.25	0.44	0.39
CG2	2702.3	876.3	32.4	1.81	0.35	0.47	0.99
CG3	2944.7	1021.4	34.69	1.79	0.41	0.31	1.07

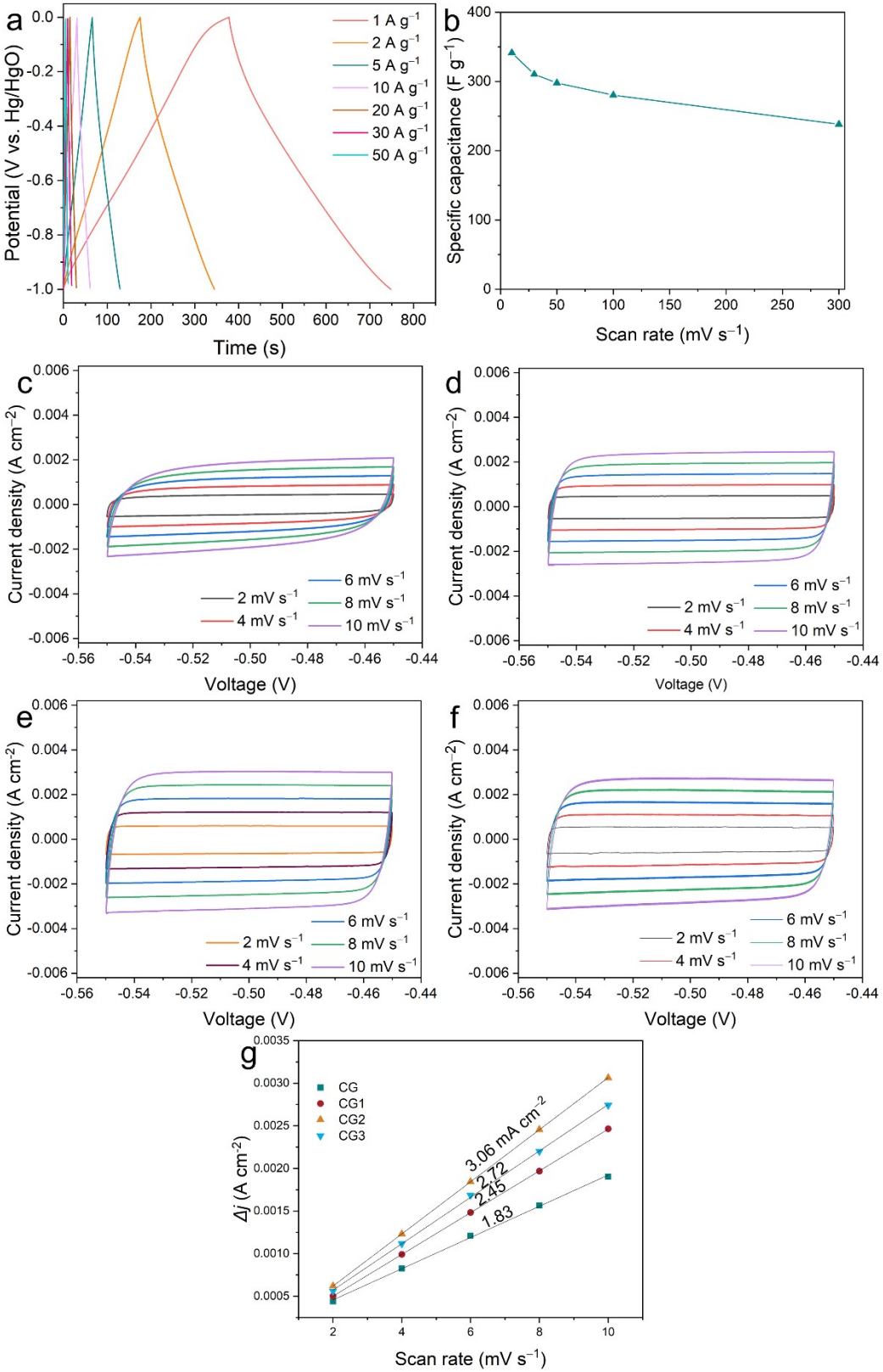

Fig. S5. (a) The GCD curves of CG2 at the current densities of 1 to 50 A g^{-1}, and (b) the specific capacitance of CG2 calculated by the CV measurement, CV curves of (c) CG, (d) CG1, (e) CG2, and (f) CG3 at the scan rate from 2 to 10 mV s^{-1}, (g) the corresponding fixed C_{dl} results of CGX electrode.

Table S2. The specific capacitance and rate ability comparison with similar materials in the recent two years.

Materials	Electrolyte	Capacitance (Current density)	Rate retention (times)	Reference
AC-TBG	1M KOH	212 F g^{-1} (1 A g^{-1})	55% (3-fold)	*Carbon* 199 (2022) 249-257 [6]
SPC-1	6M KOH	301.4 F g^{-1} (1 A g^{-1})	77.4% (20-fold)	*J. Energy Storage* 53 (2022) 105190 [7]
MLCM-750	1M H_2SO_4	338.2 F g^{-1} (0.8 A g^{-1})	70.2% (12.5-fold)	*J. Colloid Interface Sci.* 614 (2022) 566-573 [8]
N-MCNs	6M KOH	240 F g^{-1} (1 A g^{-1})	75.4% (20-fold)	*Chinese J. Chem. Eng.* 55 (2023) 34–40 [9]
NC-HPCS	6M KOH	305 F g^{-1} (0.5 A g^{-1})	78% (32-fold)	*Chem. Eng. J.* 433 (2022) 134486 [10]
BTPA-3-800	6M KOH	310.4 F g^{-1} (0.2 A g^{-1})	72.1% (20-fold）	*Int. J. Hydrogen Energy* 48 (2023) 25635-25644 [11]
fold-carbon-spheres	6M KOH	405 F g^{-1} (1 A g^{-1})	40.5% (50-fold)	*J. Colloid Interface Sci.* 630 (2023) 61-69. [12]
FLSC-4-1000	6M KOH	267 F g^{-1} (0.5 A g^{-1})	69% (10-fold)	*J. Energy Storage* 78 (2024) 110295 [13]
NCDs@HCS	6M KOH	314 F g^{-1} (1 A g^{-1})	83% (10-fold)	J. *Energy Storage* 83 (2024) 110640 [14]
FPC	6M KOH	287 F g^{-1} (1 A g^{-1})	49% (20-fold)	*J. Energy Storage* 73 (2023) 109129 [15]
HNSC	6M KOH	330.4 F g^{-1} (1 A g^{-1})	76.3% (20-fold)	*Chem. Eng. J.* 480 (2024) 148213 [16]
CG2	6M KOH	**369.8 F g^{-1}** (1 A g^{-1})	**69.0% (50-fold)**	**Our work**

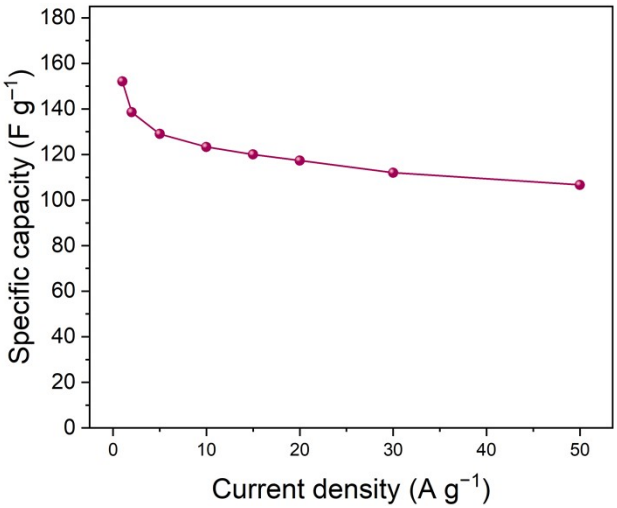

Fig. S6. The capacitance of C-G2 symmetrical supercapacitor under various current densities.

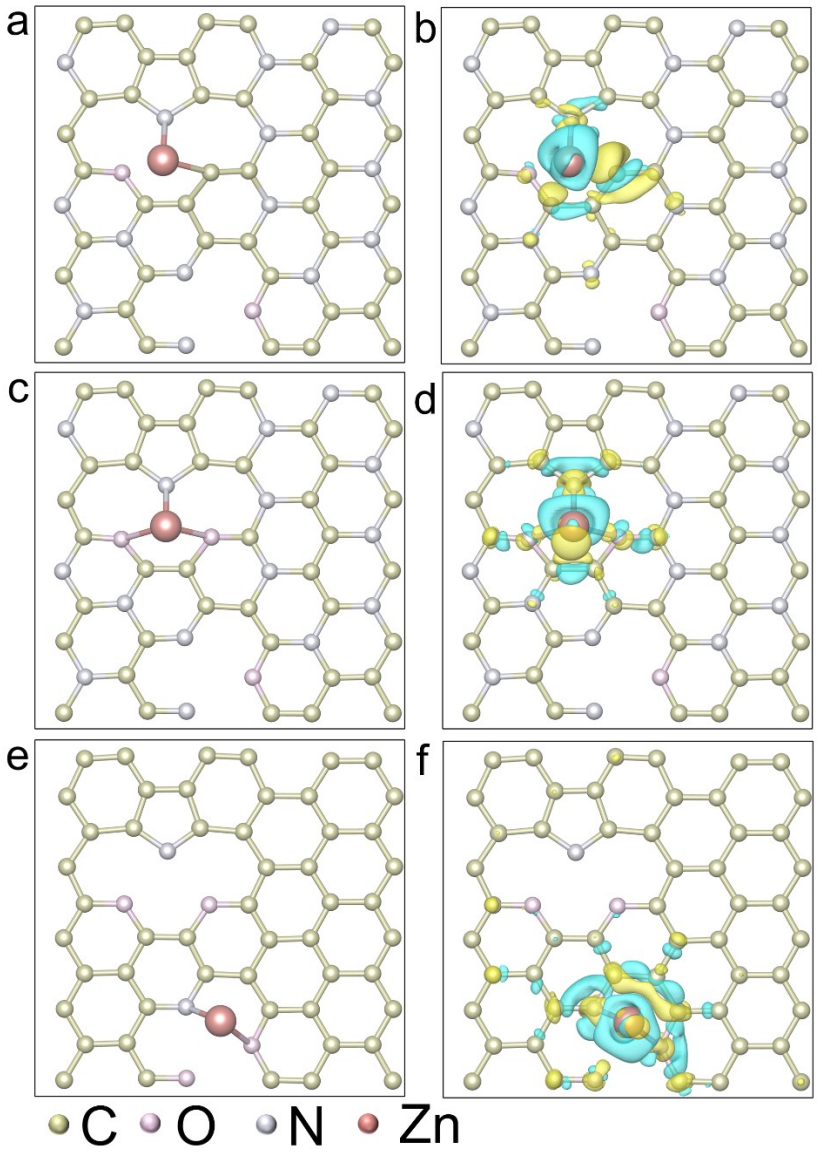

Fig. S7. The adsorption energy computational models of (a) C1, (c) C1-O-add, and (e) C2. The electron density difference results of (b) C1, (d) C1-O-add, and (f) C2.

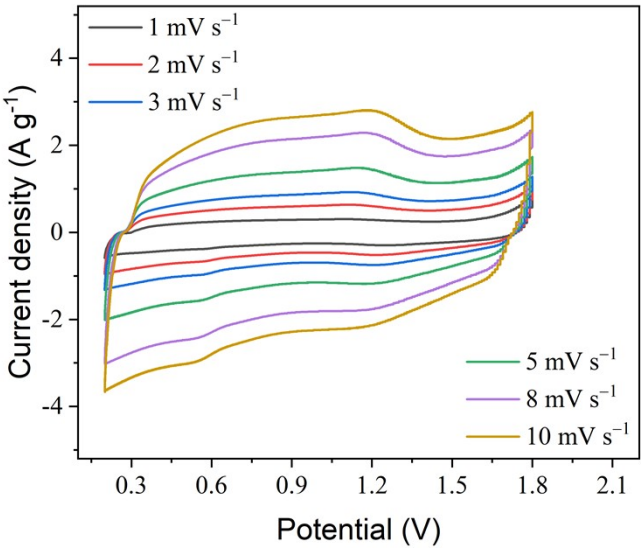

Fig. S8. CV curves of CG2 ZIC at the scan rates from 1 to 10 mV s^{-1}.

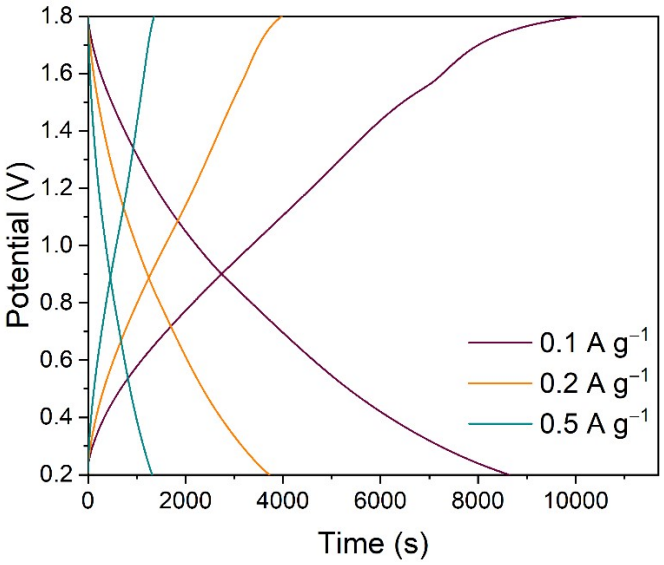

Fig. S9. GCD curves of CG2 ZIC at the current densities from 0.1 to 0.5 A g^{-1}.

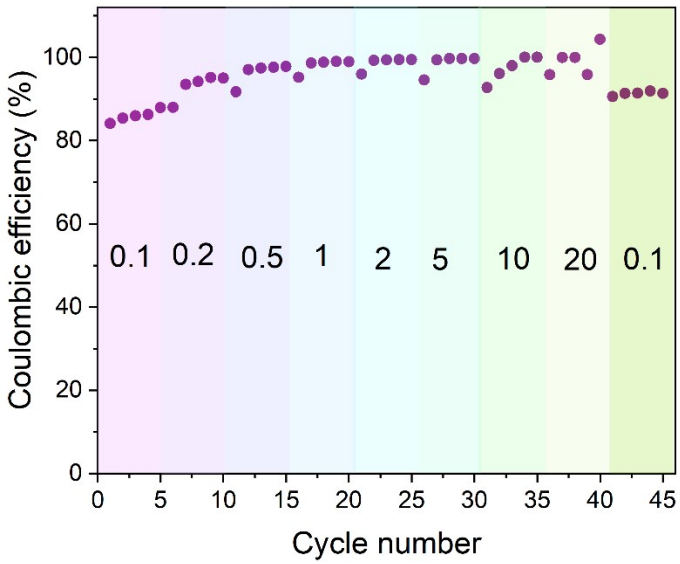

Fig. S10. The Coulombic efficiency of ZHCs at various e current densities ranging from 0.1 to 20 A g^{-1}.

Table S3. Comparison of the CG2 capacity with similar carbon materials in the recent two years.

Materials	Electrolyte	E (mAh g^{-1}) (current density)	Rate retention (current density)	Energy density (Wh kg^{-1}) @ power density	References
CG2	**1M $ZnSO_4$**	**241.1 (0.1 A g^{-1})**	**43.8% (20 A g^{-1})**	**191.6 @80 W kg^{-1}**	**This Work**
3D-Mxene	2M Zn $(CF_3SO_4)_2$	105.6 (0.2 A g^{-1})	57.8% (5A g^{-1})	104.5 @ 53.6 Wh kg^{-1}	[17]
NPFC700	1M Zn $(CF_3SO_3)_2$	207.9 (0.1 A g^{-1})	62.8% (20A g^{-1})	85.7 @ unknown	[18]
LC-750	1M $ZnSO_4$	185.3 (0.2 A g^{-1})	51.4% (10A g^{-1})	119.5 @ 20.3 kW kg^{-1}	[19]
CFe0.2	2M $ZnSO_4$	178.8 (0.5 A g^{-1})	46% (10A g^{-1})	120.2 @ 336 W kg^{-1}	[20]
CNT@PC	2M $ZnSO_4$	175.3 (0.1 A g^{-1})	53.1% (50A g^{-1})	150.8 @ 80 W kg^{-1}	[21]
SOCN	3M Zn $(CF_3SO_3)_2$	151 (0.1 A g^{-1})	50% (10 A g^{-1})	103.1 @ 51.6 W kg^{-1}	[22]
C-800	2 M $ZnSO_4$	121.7 (0.05 A g^{-1})	66.7% (20 A g^{-1})	109.3 @ 33.5 W kg^{-1}	[23]
OLDC	2 M $ZnSO_4$	136 (0.1 A g^{-1})	42.9% (20 A g^{-1})	136.3 @ 100 W kg^{-1}	[24]
S, N-CNC	2 M $ZnSO_4$	165.5 (1 A g^{-1})	40.7% (8 A g^{-1})	148.9 @ 900 W kg^{-1}	[25]
N, P-OLC	2M $ZnSO_4$	184.5 (0.5A g^{-1})	62.5% (20 A g^{-1})	149.5 @ unknown	[26]
AC-PHC	1 M $ZnSO_4$	146.4 (0.1 A g^{-1})	58% (10 A g^{-1})	117 @ 160 W kg^{-1}	[27]
SN-PCNTs	2 M $ZnSO_4$	152.6 (0.2 A g^{-1})	44.5% (40 A g^{-1})	95.9 @ 125 W kg^{-1}	[28]
DCP	2 M $ZnSO_4$	140 (0.2 A g^{-1})	61.6% (6.4 A g^{-1})	111.1 @ unknown	[29]
FPC	1 M Zn $(CF_3SO_3)_2$	135.5 (1 A g^{-1})	67.5% (10 A g^{-1})	121.95 @ 900 W kg^{-1}	[15]
OMC30	1M $ZnSO_4$	242.0 (0.25 A g^{-1})	25.2% (2 A g^{-1})	206.1 @ 212.5 W kg^{-1}	[30]
HC-800	0.5 M Na_2SO_4+1 M Zn $(CF_3SO_3)_2$	242.25 (0.5 A g^{-1})	44.68% (50A g^{-1})	186.1 @ unknown	[31]
IMCC	1 M $Zn(CF_3SO_3)_2$	177 (0.5 A g^{-1})	40.7% (20 A g^{-1})	44.2 Wh cm^{-2} @ 29.77 mW cm^{-2}	[32]
NPHC	1M $ZnSO_4$+DT	123.5 (0.1 A g^{-1})	48.6% (10A g^{-1})	/	[33]

References

[1] G. Kresse, J. Furthmuller, Efficient iterative schemes for ab initio total-energy calculations using a plane-wave basis set, Phy. Rev. B, 54 (1996) 11169-11186.

[2] G. Kresse, J. Furthmuller, Efficiency of ab initio total energy calculations for metals and semiconductors using a plane-wave basis set, Comput. Mater. Sci. 6 (1996) 15-50.

[3] J. P. Perdew, K.Burke, M. Ernzerhof, Generalized Gradient Approximation Made Simple, Phy. Rev. Lett. 77 (1996) 3865-3868.

[4] G. Kresse, D. Joubert, From Ultrasoft Pseudopotentials to the Projector Augmented Wave Method, Phy. Rev. B, 59 (1999) 1758-1775.

[5] S. Grimme, J. Antony, S. Ehrlich, H. Krieg, A consistent and accurate ab initio parametrization of density functional dispersion correction (DFT-D) for the 94 elements H-Pu, J. Chem. Phy. 132 (2010) 154104.

[6] T. Prasankumar, D. Salpekar, S. Bhattacharyya, K. Manoharan, R.M. Yadav, M.A. Campos Mata, K.A. Miller, R. Vajtai, S. Jose, S. Roy, P.M. Ajayan, Biomass derived hierarchical porous carbon for supercapacitor application and dilute stream CO_2 capture, Carbon, 199 (2022) 249-257.

[7] Y. Chen, X. Xu, R. Ma, S. Sun, J. Lin, J. Luo, H. Huang, Preparation of hierarchical porous carbon by pyrolyzing sargassum under microwave: The internal connection between structure-oriented regulation and performance optimization of supercapacitors, J. Energy Storage, 53 (2022) 105190.

[8] C. Liu, Y. Hou, Y. Li, H. Xiao, Heteroatom-doped porous carbon microspheres derived from ionic liquid-lignin solution for high performance supercapacitors, J. Colloid Interface Sci. 614 (2022) 566-573.

[9] J. Du, A. Chen, S. Hou, X. Gao, Self-deposition for mesoporous carbon nanosheet with supercapacitor application, Chinese J. Chem. Eng. 55 (2023) 34-40.

[10] S. Park, B. Seo, D. Shin, K. Kim, W. Choi, Sodium-chloride-assisted synthesis of nitrogen-doped porous carbon shells via one-step combustion waves for supercapacitor electrodes, Chem. Eng. J. 433 (2022) 134486.

[11] Q. Xu, X. Ni, S. Chen, J. Ye, J. Yang, H. Wang, D. Li, H. Yuan, Hierarchically porous carbon from biomass tar as sustainable electrode material for high-performance supercapacitors, Int. J. Hydrogen Energy, 48 (2023) 25635-25644.

[12] J. Du, M. Li, J. Song, X. Gao, S. Hou, A. Chen, In-situ activator-induced evolution of morphology on carbon materials for supercapacitors, J. Colloid Interface Sci. 630 (2023) 61-69.

[13] C. Zhao, X. Tong, Y. Yang, H. Guo, W. Gao, M. Li, Y. Zhu, C. Zhao, Loofah sponge-derived 3D flexible porous carbon electrode for high performance supercapacitor, J. Energy Storage, 78 (2024) 110295.

[14] J. Dai, G. Li, Y. Hu, L. Han, Hollow carbon spheres anchored with nitrogen-doped carbon dots for high-performance supercapacitors, Journal of Energy Storage, 83 (2024) 110640.

[15] W. Tian, P. Ren, X. Hou, Z. Guo, Z. Chen, Y. Jin, Construction of N-doped mesoporous carbon via micelle-induced chitosan for enhancing capacitive storage, J. Energy Storage, 73 (2023) 109129.

[16] Z. Ji, G. Tang, L. Chen, J. Zhong, Y. Chen, G. Zhu, X. Chuan, J. Zhang, X. Shen, Defect engineering of hollow porous N, S co-doped carbon spheres-derived materials for high-performance hybrid supercapacitors, Chem. Eng. J. 480 (2024) 148213.

[17] F. Li, Y.-l. Liu, G.-G. Wang, S.-Y. Zhang, D.-Q. Zhao, K. Fang, H.-Y. Zhang, H.Y. Yang, 3D porous H-Ti3C2T films as free-standing electrodes for zinc ion hybrid capacitors, Chem. Eng. J. 435

(2022) 135052.
[18] F. Wei, Y. Wei, J. Wang, M. Han, Y. Lv, N, P dual doped foamy-like carbons with abundant defect sites for zinc ion hybrid capacitors, Chem. Eng. J. 450 (2022) 137919.
[19] H.-X. Li, W.-J. Shi, L.-Y. Liu, X. Zhang, P.-F. Zhang, Y.-J. Zhai, Z.-Y. Wang, Y. Liu, Fabrication of dual heteroatom-doped graphitic carbon from waste sponge with "killing two birds with one stone" strategy for advanced aqueous zinc–ion hybrid capacitors, J. Colloid Interface Sci. 647 (2023) 306-317.
[20] L. Huang, Z. Gu, W. He, K. Shi, L. Peng, Z. Sheng, F. Zhang, W. Feng, H. Liu, Solvothermal Synthesis and Pyrolysis Toward Heteroatom-Doped Carbon Microspheres for Zinc-Ion Hybrid Capacitors, Small, 20 (2023) 2308788.
[21] B. Yang, W. Zhao, Z. Gao, J. Yang, W. Shi, Y. Zhang, Q. Su, B. Xu, G. Du, Flexible CNT@Porous carbon sponge cathode with large mesopores for high-rate zinc-ion hybrid capacitors, Carbon, 218 (2024) 118695.
[22] C. Zhu, R. Long, L. Zhu, W. Zou, Y. Zhang, Z. Gao, J. Shi, W. Tian, J. Wu, H. Wang, Sulfate template induced S/O doped carbon nanosheets enabling rich physi/chemi-sorption sites for high-performance zinc ion hybrid capacitors, J. Colloid Interface Sci. 652 (2023) 590-598.
[23] F. Wei, H. Tian, P. Chen, Y. Lv, J. Huang, Construction of porous carbon nanosheets by dual-template strategy for zinc ion hybrid capacitor, Appl. Surf. Sci. 613 (2023) 156021.
[24] H. Li, P. Su, Q. Liao, Y. Liu, Y. Li, X. Niu, X. Liu, K. Wang, Olive Leaves-Derived Hierarchical Porous Carbon as Cathode Material for Anti-Self-Discharge Zinc-Ion Hybrid Capacitor, Small, 19 (2023) 2304172.
[25] H. Gupta, Y. Dahiya, H.K. Rathore, K. Awasthi, M. Kumar, D. Sarkar, Energy-Dense Zinc Ion Hybrid Supercapacitors with S, N Dual-Doped Porous Carbon Nanocube Based Cathodes, ACS Appl. Mater. Interfaces, 15 (2023) 42685-42696.
[26] H. Wang, Q. Chen, P. Xiao, L. Cao, Unlocking Zinc-Ion Energy Storage Performance of Onion-Like Carbon by Promoting Heteroatom Doping Strategy, ACS Appl. Mater. Interfaces, 14 (2022) 9013-9023.
[27] X. Zhang, X. Tian, Y. Song, J. Wu, T. Yang, Z. Liu, High-performance activated carbon cathodes from green cokes for Zn-ion hybrid supercapacitors, Fuel, 310 (2022) 122485.
[28] J. Li, L. Yu, W. Wang, X. He, G. Wang, R. Liu, X. Ma, G. Zhang, Sulfur incorporation modulated absorption kinetics and electron transfer behavior for nitrogen rich porous carbon nanotubes endow superior aqueous zinc ion storage capability, J. Mater. Chem. A, 10 (2022) 9355-9362.
[29] L. Liu, Z. Sun, Y. Lu, J. Zhang, Y. Li, G. Zhang, X. Chen, S. Omanovic, S. Sun, H. Song, d-Calcium pantothenate-derived porous carbon: carbonization mechanism and application in aqueous Zn-ion hybrid capacitors, J. Mater. Chem. A, 11 (2023) 14311-14319.
[30] A. Yu, Y. Zhao, W. Zhang, W. Yang, L. Zhu, P. Peng, F.F. Li, Y. Yang, Bi-Directional Electrolytic Reduction of CO_2 to Mesoporous Carbons with Regulated Structure and Surface Functional Groups for Zn-ion Capacitors, Adv. Funct. Mater. 34 (2023) 2309666.
[31] M. Zou, X. Li, S. Luo, J. Chen, M. Hou, G. Gao, High-performance aqueous zinc ion hybrid capacitors obtained by Na2SO4 additive and dense pore structure, Nanoscale, 15 (2023) 11681.
[32] W. Luo, N. Guo, L. Wang, D. Jia, M. Xu, S. Zhang, L. Ai, R. Sheng, S. Feng, X. Gong, Y. Cao, Homogeneous activation induced by bacterial cellulose nanofibers to construct interconnected microporous carbons for enhanced capacitive storage, J. Colloid Interface Sci. 636 (2023) 33-41.
[33] H. Peng, X. Wang, F. Yang, Z. Liu, H. Lei, S. Cui, X. Xie, G. Ma, Regulating solvation structure and inducing Zn (002) plane by a multifunctional electrolyte additive toward dendrite suppression and

long-life zinc ion hybrid capacitors, Chem. Eng. J. 474 (2023) 145864.